S1   Definition of NO$_y$

For the comparison between the aircraft in situ measurements and the model results we use the following definition of NO$_y$:

$$NO_y = N + NO_2 + NO + HNO_3 + HNO_4$$
$$+ HONO + 2xN_2O_5 + PAN + HNO + ISON$$
$$+ LC_4H_9NO_3 + IC_3H_7NO_3$$
$$+ BrNO_2 + BrNO_3 + ClNO_2$$
$$+ ClNO_3$$

Please note that the definition of the NO$_y$ family used by the TAGGING method differs slightly, because PAN is tagged individually due to the large importance of PAN for long range transport (see Grewe et al., 2017).

S2   Total emissions

Table S1 lists the annual total NO$_x$ emissions of the considered emission sectors on the global scale.

emission sector	Global	EU	NA	EA	ROW
Land transport	21.7	2.6 (0.7)	4.3 (1.1)	4.5 (1.1)	10.3 (2.5)
Non-traffic	43.5	3.9 (1.1)	5.2 (1.3)	14.9 (3.6)	19.5 (4.7)
Shipping	12.6				
BB + AWB	8.2				
Soil-NO$_x$	13.0				
Lightning	12.1				

Table S1. Totals of NO$_x$ emissions (in Tg(NO) a^{-1}) for the applied emission sectors. For the emission sectors land transport and anthropgenic non-traffic distinguish in addition various geographical source regions, which are: globally, in Europe (EU), in North America (NA), in East Asia (EA) and in the rest of the world (ROW). The emissions are given for 2017 and JJA 2017 in parentheses. BB is short for Biomass Burning and AWB is short for Agricultural Waste Burning

S2.1   Biogenic Emissions

Figures S1 and S2 depict the seasonal (JJA) mean fluxes of biogenic C$_5$H$_8$ and soil-NO$_x$.
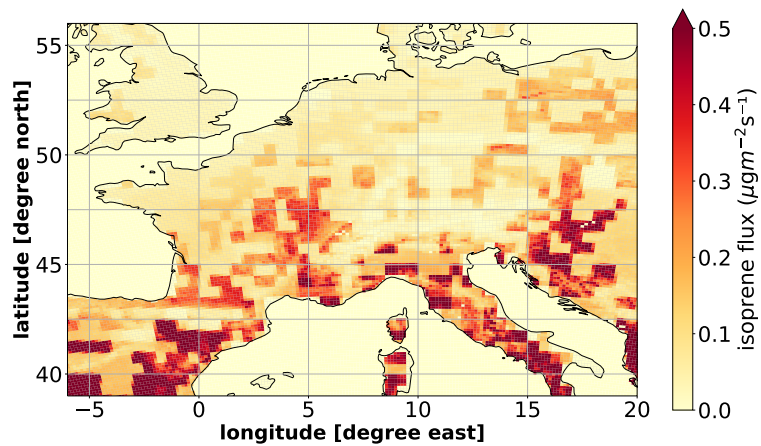
Figure S1. Seasonal (JJA 2017) mean of the isoprene (C_5H_8) emission flux in μg m^{-2}s^{-1} as simulated by CM12.
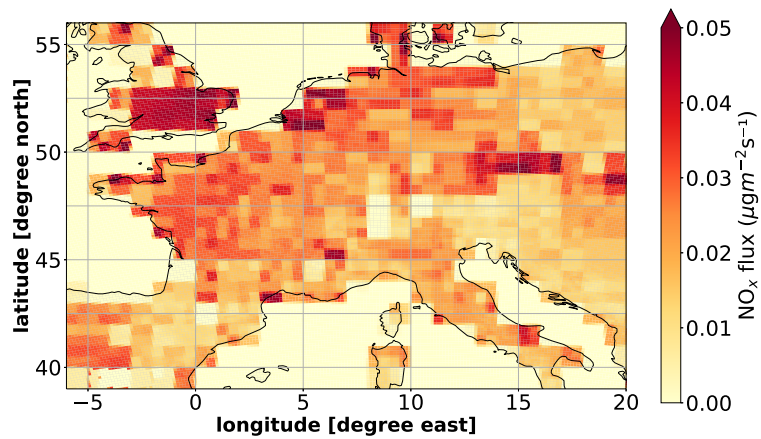

Figure S2. Seasonal (JJA 2017) mean of the soil NO_x emission flux in μg m^{-2}s^{-1} as simulated by CM12.

S2.2 Emissions in the study regions

15 Table S2 lists the seasonal (JJA) mean emission flux of various emission sectors averaged over the considered regions.

Region	NO_x^{teu}	NO_x^{soil}	C_5H_8
unit	ng(N) m^{-2} s	ng(N) m^{-2} s	ng(C) m^{-2} s
Benelux	21.7	7.6	7.0
Po Valley	12.1	4.7	32.1
Iberian Peninsula	5.1	3.9	60.1
Ireland	1.1	2.6	0.7

Table S2. Seasonal mean (JJA 2017) emission fluxes from land transport (teu), soil-NO_x and biogenic isoprene in the various study regions.

S3   Online flagging of emissions

To subdivide the global emission flux files, which are used as input of the model, into regional subsets corresponding to the individual regions, we applied the SCALC (Simple CALCulations) submodel. Kern (2013) describes the submodel in detail, which allows the multiplication of two channel objects, here applied in order to prepare the emissions for the tagging by the source regions (see Appendix C in Kern, 2013). The anthropogenic emission inventory EDGAR v5.0 is multiplied with flags from files containing 1 for a specific tagging region, and 0 everywhere else. This defines new channel objects with emission fluxes, where emissions are non-zero in the tagged region and set to zero everywhere else. For the present study the simple multiplication has been further expanded to ensure that all emissions, also along coastlines, are conserved.

S4   Pre-processing of EDGAR

During the preparation of the EDGAR emissions, the different sectors from EDGAR are mapped on a simplified sector definition containing the sectors anthropogenic non-traffic, land transport and shipping. During the summation of the sectors, each sub-sector of EDGAR is vertically distributed according to Mailler et al. (2013). Table S3 shows the vertically distributed fraction for each level and each emission sector. In the pre-processing the distribution onto 7 levels was achieved, by multiplying the emission flux at each grid point with a vector containing the individual fractions (Table S3).

SNAP sectors[1]										
Level [m]	1	2	3	4	5	6	7	8	9	10
0	0.	11.	0.	20.	20.	100	100	100	2.	100
20	0.	89.	21.3	70.	70.	0.	0.	0.	8.	0.
92	0.25	0.	75.4	7.	6.	0.	0.	0.	37.	0.
184	51.	0.	3.3	1.	3.	0.	0.	0.	51	0.
324	45.3	0.	0.	0.	0.	0.	0.	0.	2.	0.
522	3.29	0.	0.	0.	0.	0.	0.	0.	0.	0.
781	0.2	0.	0.	0.	0.	0.	0.	0.	0.	0.

Table S3. Vertical distribution (fractions in (%) per European Monitoring and Evaluation Programme (EMEP) levels in m (left column) and per SNAP sectors from Bieser et al. (2011), with an additional 0–20 m layer for surface emissions (adapted from, Mailler et al., 2013). [1]SNAP sectors: 1. combustion in energy and transformation industry, 2. non-industry combustion, 3 .comb. in manufacturing industry, 4. prod. processes, 5. extraction of fossil fuels, 6. solvent use, 7. road transport, 8. other mobile sources, 9. waste treatment, 10. agriculture, 11. other sources and sinks.

S5   Pre-processing of GFAS

The biomass burning emissions in our simulations are prescribed based on the GFAS data set from the ECMWF CAMS. In order to represent the dispersion of biomass burning emissions by the pyro-convection in an appropriate way, we pre-processed the GFAS emissions to vertically distribute them onto 6 levels up to 4500 m depending on their geographical location (Dentener et al., 2006, see Table S4).

S6   Evaluation

For the model evaluation we focus on the results of CM12, as we will use these results mostly for the further analyses. Nevertheless, some evaluations can only be performed with CM50, as longer time periods are needed. Therefore, we compare in a first step ground-level O_3 between CM50 and CM12 for the summer months JJA 2017 and transformed the data of CM12 on

		Level [m]					
Region		50	300	750	1500	2500	4500
tropical (30 S-30 N)		20.	40.	40.	0.	0.	0
Temperate (30 N-60 N, 30 S-60 S)		20.	20.	20.	40.	0.	0
Boreal (Eurasia)		10.	10.	20.	20.	40.	0
Boreal (Canada)		10.	10.	10.	10.	20.	40

Table S4. Fractional distribution (in %) of emission heights for wild-land fires (Dentener et al., 2006, from). Contributions assigned to heights below the actual surface altitude are moved into the lowest applicable height range, and contributions of the 0-100m altitude are always emitted into the lowest model layer.

the grid of CM50 (Figure S3). Generally, CM50 and CM12 simulate the same order of magnitude and a similar geographical
40 distribution of ground-level O_3.

S6.1 TOAR dataset

In order to evaluate ground-level O_3 simulated by the MECO(n) model in Europe, the CM50 model results are compared with the data product (further denoted as D21) created by Delang et al. (2021). The data product contains the seasonal ozone daily maximum 8 h mixing ratio (OSDMA8), which is based on the maximum 8-hourly running mean ozone values (MDA8).
45 They combined a large number of O_3 measurements at various stations from the TOAR database with results from nine different atmospheric chemistry models (Delang et al., 2021). The atmospheric chemistry model simulations mostly stem from phase one of the Chemistry-Climate Model Initiative (CCMI). In order to create a multimodel composite of all nine atmospheric chemistry models, M^{3}Fusion was used (Delang et al., 2021). M^{3}Fusion corrects the model bias and finds a linear combination of models in each region and year that minimizes the mean square error as compared to observations (Delang
50 et al., 2021). The hourly surface ozone observations cover 1970 to 2015, for 2016 and 2017 fewer data are available compared to 2015. For the analyses we first calculate the seasonal ozone daily maximum 8 h mixing ratio (OSDMA8) in CM50 and interpolate the results onto the (coarser) grid of D21. By calculating the area weighted differences between CM50 and D21, ignoring the missing data points, we calculate a mean bias of 16.5 nmol mol^{-1}.
Figure S4 displays ground-level OSDMA8 in nmol mol^{-1} for CM50 (upper panel) and the ground-level OSDMA8 in nmol mol^{-1}
55 from the D21 data product in 2017 (middle panel). The lower panel in Figure S4, shows the differences between CM50 and D21 onto the D21 grid. Here, the CM50 results have been reduced by the mean bias of 16.5 nmol mol^{-1}. The figure indicates that in CM50 O_3 is systematically overestimated with a bias of 16–20 nmol mol^{-1} in rural regions like the Alps, parts of the Iberian Peninsula, Wales, and the Balkan region. The ozone bias in polluted areas like the Ruhr area, Benelux, parts of France and the Po Valley and in the range of 5–10 nmol mol^{-1}.
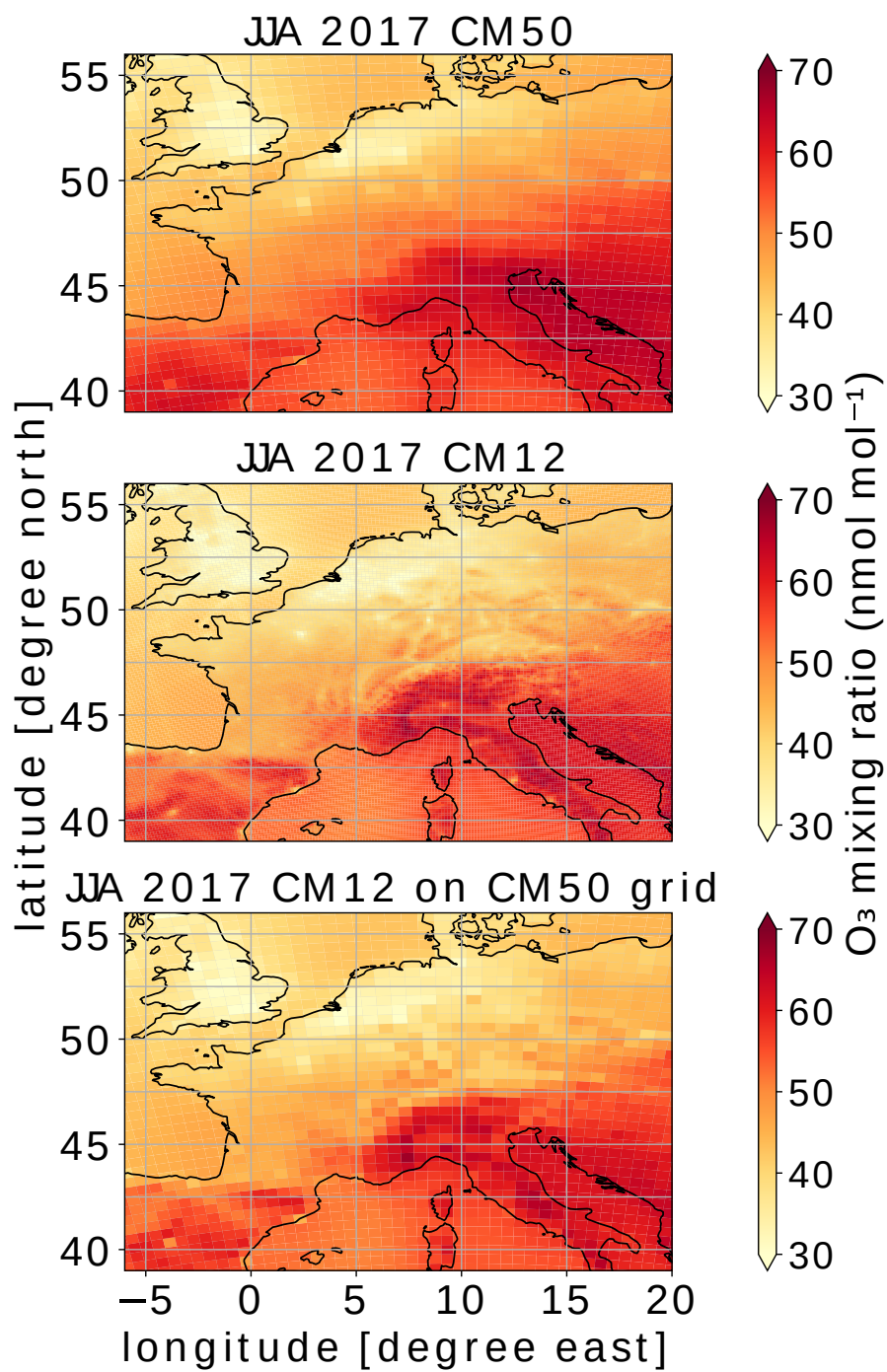
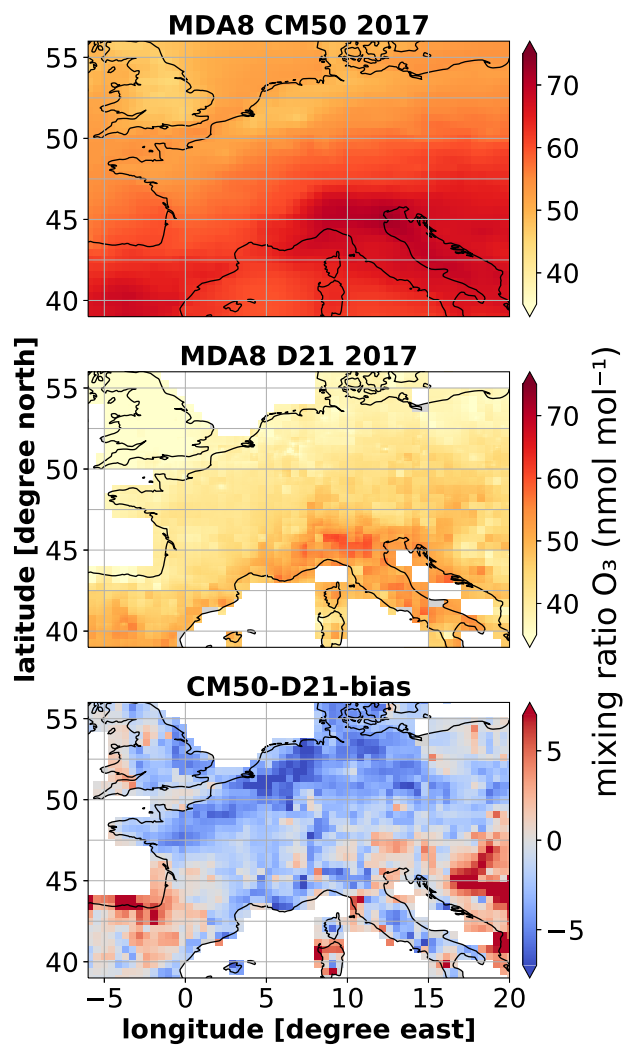**Figure S3.** Comparison of ground-level ozone for JJA 2017 between CM50 (50 km) and CM12 (12 km).

Figure S4. Comparison of the 6-month mean of the daily maximum 8-hour ground-level O_3 mixing ratio (nmol mol^{-1}) for 2017 of CM50 (0.44° x 0.44°) with D21. White areas in D21 are missing values. For the difference of CM50 and D21 the CM50 results have been di-biased as described in the text.

S6.2 Ground-level observations

In order to evaluate simulated ground-level O_3 concentrations, a comparison with observational data from the AirBase network was performed. AirBase is a European air quality database, maintained by the EEA (European Environment Agency: https://www.eea.europa.eu/data-and-maps/data/aqereporting-8) through its European topic centre on Air pollution and Climate Change mitigation (European Environment Agency, 2018). The database contains air quality monitoring data and information submitted by participating countries throughout Europe. As regional models are typically not able to capture conditions near strong sources (e.g. measurements at traffic sites or near industrial sites), we restrict the evaluation to stations labeled as 'background'. Negative concentrations in the measurement data have been eliminated; missing values are not considered during the evaluation process. In order to compare the model results with the measurements, we sample the model data using a nearest neighbor approach from hourly model output of CM12.

Figures S5 and S6 show the probability density functions (PDFs) of NO_x and O_3 at 287 (NO_x) and 386 (O_3) measurement stations in Europe for JJA 2017, respectively. The comparison reveals that the frequency of observed NO_x concentrations below 3 µg m^{-3} are overestimated by CM12 (blue line), whereas that for large NO_x concentrations is underestimated. While the frequency of large NO_x is underestimated, there is an overall positive simulation bias of the frequency of O_3. The model overestimates the frequency of small ozone values and underestimates the frequency of very large ozone values.
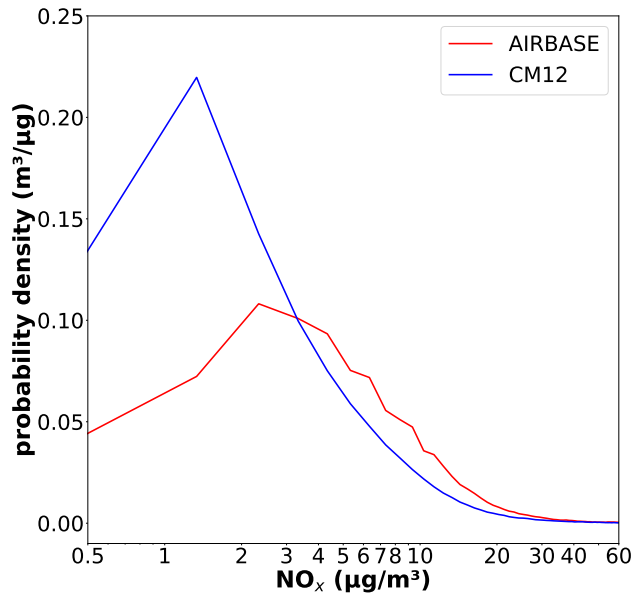

Figure S5. Probability density function for JJA 2017 of the hourly ground-level NO_x concentrations in µg m^{-3} of the model output of CM12 (blue) and the rural AIRBASE station data (red).

S6.3 HALO in situ measurements from EMeRGe Europe

The flight measurement campaign EMeRGe Europe took place in July 2017 with HALO flights across Europe. The goal was to measure emission plumes from major polluted regions and to study their transport and transformation (Andrés Hernández et al., 2022). Since the focus of our study is on ozone and NO_y, the respective in situ measurement data from EMeRGe Europe were used for comparison. A detailed description of the instruments can be found in Andrés Hernández et al. (2022) and Ziereis et al. (2022). In our study, three flights (11.07.2017, 20.07.2017 and 26.07.2017) are analysed, because these flights took place within our study areas (Po Valley and Benelux). In order to facilitate the evaluation of the MECO(n) model with
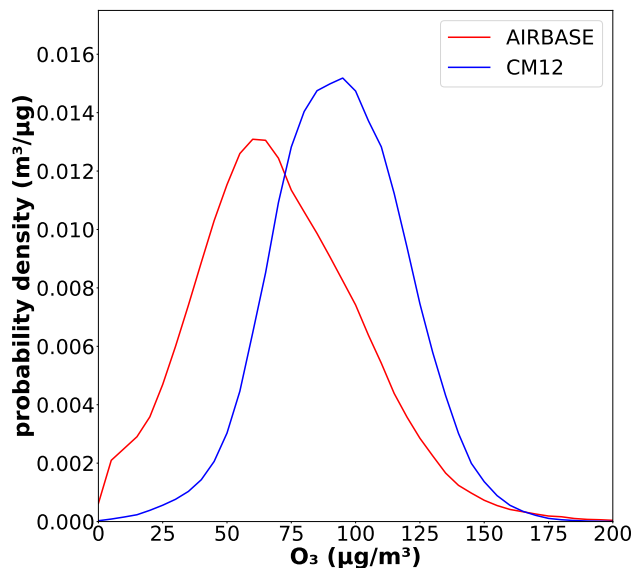
Figure S6. Probability density function for JJA 2017 of the hourly mean ground-level O_3 concentrations in µg m^{-3} of the model output of CM12 (blue) and the rural AIRBASE station data (red).

these flight data, the "sampling in 4 dimensions" (S4D) submodel is used. S4D allows to sample on-line the MECO(n) model output along the flight position at the highest possible frequency, i.e. at every model timestep (Jöckel et al., 2010).
A detailed inter-comparison between aircraft in situ measurements and model data is limited. Specific features in the model
85   could be shifted in time (or space) compared to the observations (see also discussion by Andrés Hernández et al., 2022). Therefore, we will here focus on a more qualitative comparison between the measurements and the model results for the specific flights and regions. More quantitative scatter plots are part of the manuscript.

S6.3.1   Po Valley

Figure S7 depicts the comparison of the observational data with CM12 model results for the Po Valley on the 11th of July
90   2017 for NOy (upper panel) and O_3 (lower panel). It indicates that NO_y at 725 hPa (left panel) is well represented by the model and observed enhancements of NO_y west of Genoa are reproduced by the model. The NO_y outflow of the Po Valley west of Venice at 925 hPa agrees geographically and temporally very well (right panel). Compared to NO_y, O_3 is mostly overestimated, as shown for the pressure levels at 725 hPa and 925 hPa, respectively. This confirms the findings based on the intercomparison with the D21 data set and the ground-level observations.
95   The vertical profiles of NO_y and O_3 displayed in Figures S8 confirm the agreement between measurement and observations for NO_y. Further, it confirms the overestimation of O_3 at 725 hPa in CM12 and shows large O_3 values above 700 hPa, which have not been measured by HALO. This overestimation is caused by a large scale transport of O_3 rich airmasses from France to Northern Italy simulated by MECO(n).
For the flight across the Po Valley, taking place on July 20th, 2017, the simulated geographical distributions of the NO_y plumes
100   at 925 hPa agree with the observations. In this case, however, NO_y is mainly underestimated by the model near city centres (Milano plume). At the same time, O_3 is mainly underestimated by the model near these city plumes, while it agrees well with the observations outside the plumes (see Figs. S9 and S10).
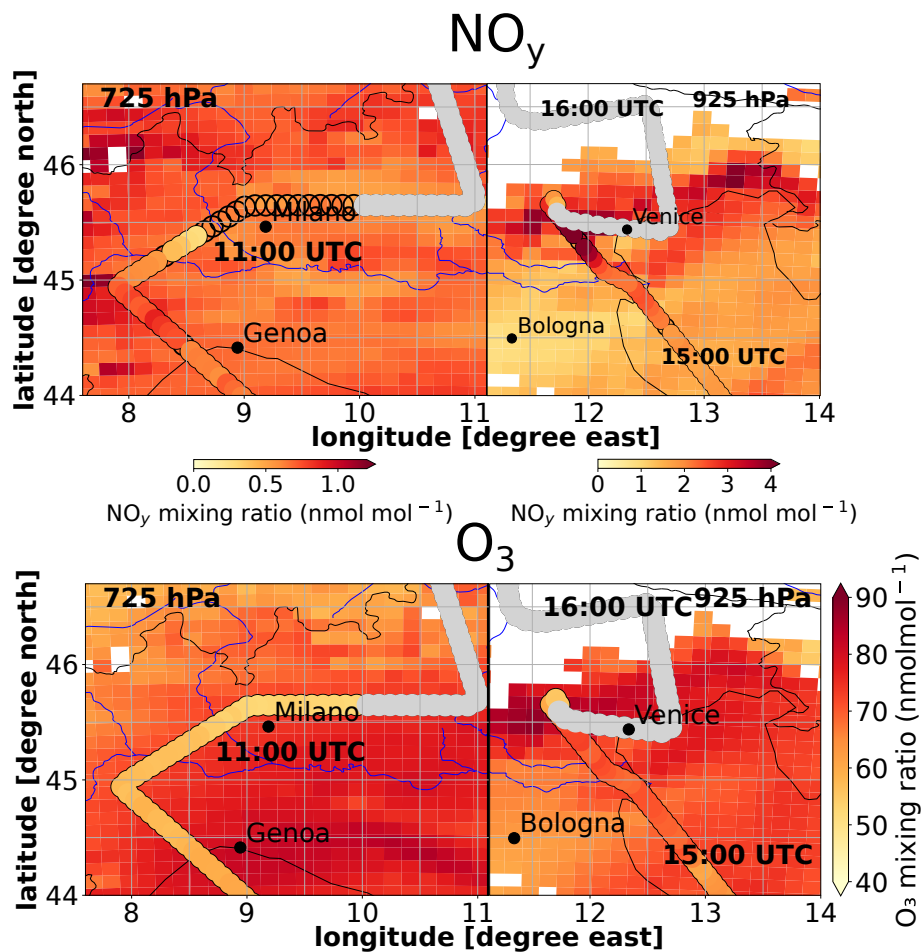
9

Figure S7. NO_y (upper panel) and O_3 (lower panel) mixing ratios in $\mathrm{nmol\,mol^{-1}}$ of the model output of CM12 (background color) at 725 hPa (11 UTC) and 925 hPa (15 UTC) and the HALO in situ measurements (filled circles) for the flight date 11.07.2017 in the Po Valley. The grey filled circles mask the measurement data, where HALO flew above or below the shown pressure level. The white spots mark the grid points in which the surface pressure is lower than 725 hPa (left) and 925 hPa (right), respectively. Unfilled circles mark missing data.

Figure S8. Comparison between CM12 model results sampled along the flight path of HALO (background color) with the HALO in situ measurements (filled circles) for the flight date 11.07.2017 in the Po Valley. Unfilled circles mark missing data. Shown are comparisons of the mixing ratios of NO_y (upper panel) and O_3 (lower panel) for two different time periods (left and right panel). All mixing ratios are given in $nmol\ mol^{-1}$. Please note different colour scales on the individual figures.
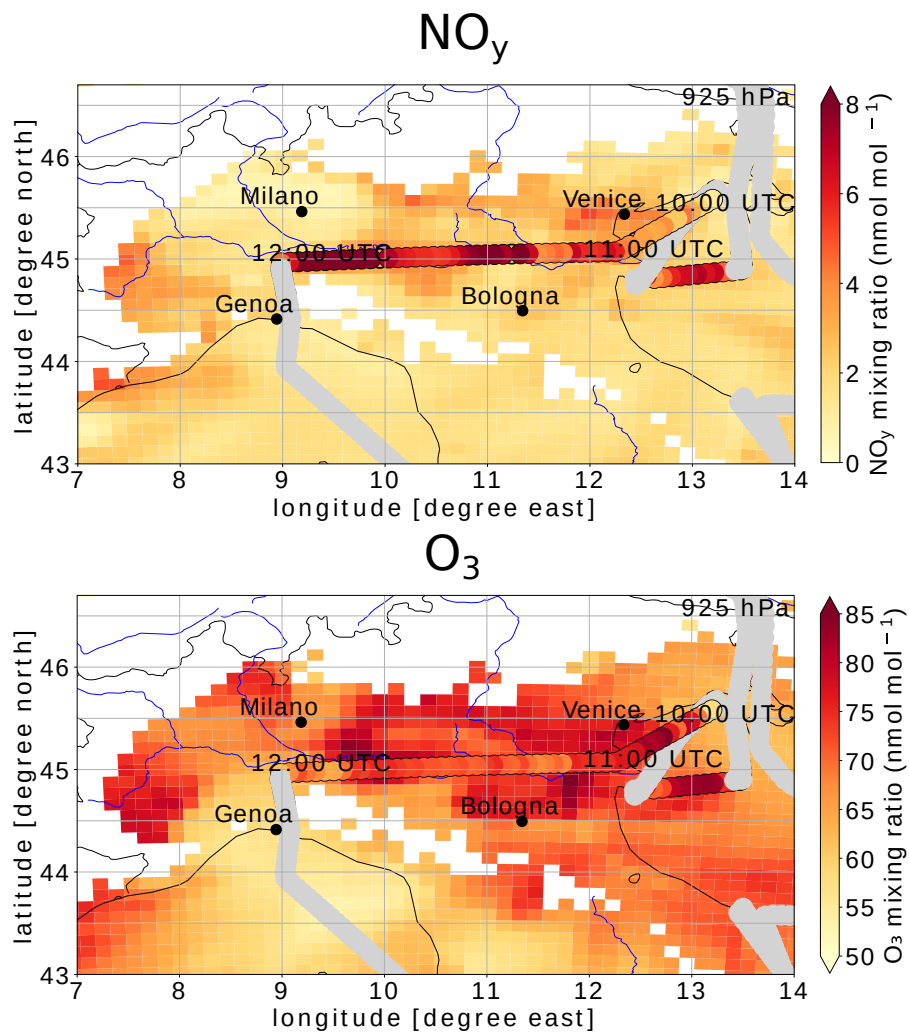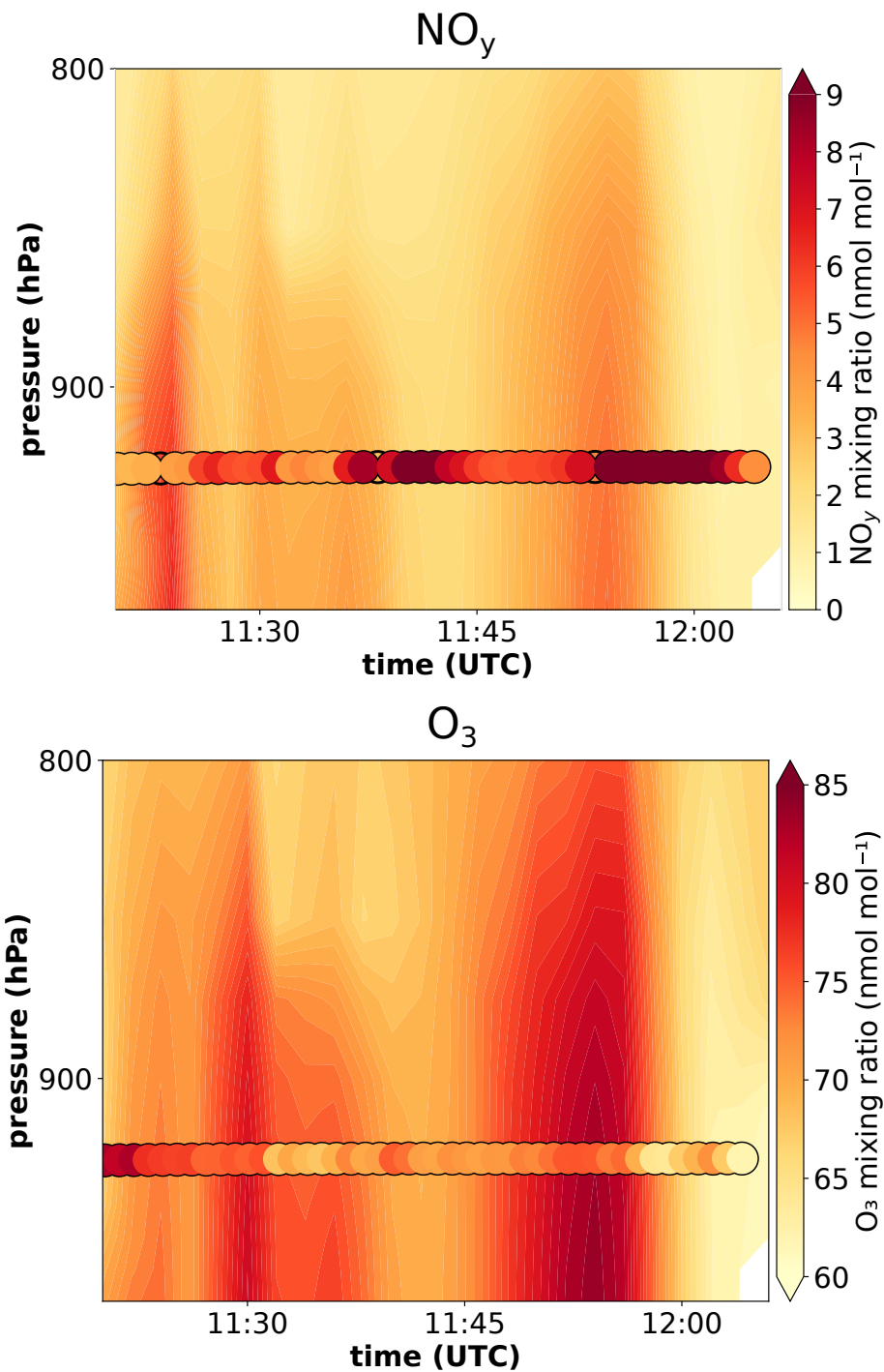
Figure S9. Comparison between NO_y (upper panel) and O_3 (lower panel) mixing ratios as simulated by CM12 sampled along the flight path of HALO (background color) with the HALO in situ measurements (filled circles) for the flight date 20.07.2017 in the Po Valley.

Figure S10. Comparison between NO_y (upper panel) and O_3 (lower panel) mixing ratios as simulated by CM12 sampled along the flight path of HALO (background color) with the HALO in situ measurements (filled circles) for the flight date 20.07.2017 in the Po Valley.

S6.3.2 Benelux

Figure S11 displays the measurements from the flight in the Benelux region on July 26th, 2017 in a composite with CM12
105 data. The NO_y plume of Antwerp is shifted northward in the CM12 simulation results. NO_y is mostly underestimated in the neighborhood of city centres. In between the city plumes, NO_y is well represented by CM12. At the same time O_3 is underestimated within plumes, especially between Bruges and Antwerp large O_3 mixing ratios are placed too far to the East by CM12. Outside the city plume, starting at 12:50 UTC, O_3 is very well represented by CM12, which is confirmed by the vertical profiles (Fig. S12). Overall, CM12 is able to capture the variations of NO_y and O_3 mixing ratios measured during the
110 aircraft in situ measurements. Specific patterns, however, are shifted in time and space. There is a tendency that in the neighborhood of city centres and in their downwind plumes, the model results partly underestimate NO_y and under-/overestimate O_3.
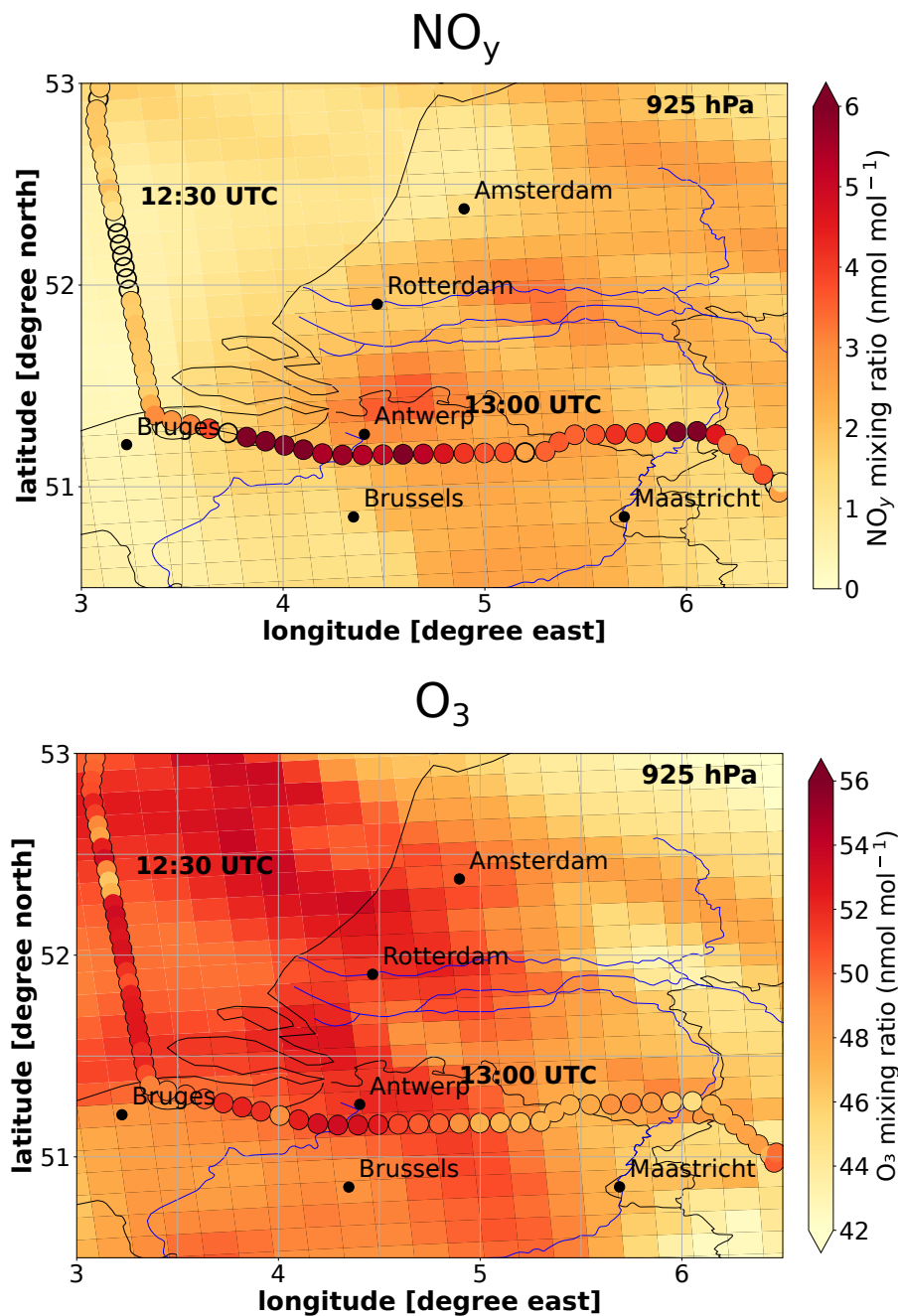
Figure S11. Comparison between model results of O_3 mixing ratios in nmol mol^{-1} sampled along the flight path of CM12 (background color) with the HALO in situ measurements (filled circles) for the flight date 26.07.2017 in the Benelux region.
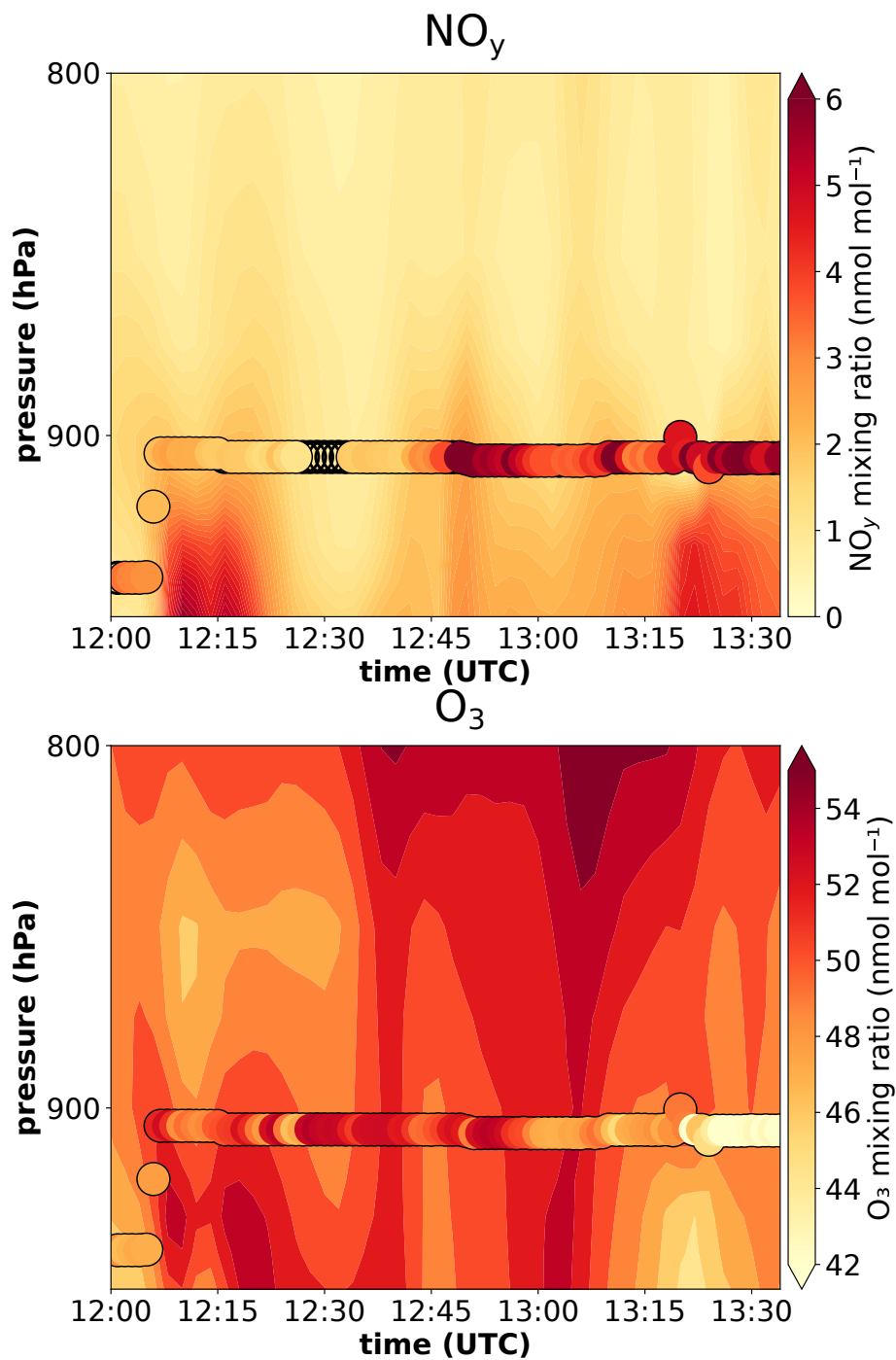
Figure S12. Comparison between CM12 model results sampled along the flight path of HALO (background color) with the HALO in situ measurements (filled circles) for the flight date 26.07.2017 over Benelux. Unfilled circles mark missing data. Shown are comparisons of the mixing ratios of NO_y (upper panel) and O_3 (lower panel). All mixing ratios are given in nmol mol^{-1}.

S7   Comparison of ozone and contributions between 2017 and 2018

Figure S13 shows a comparison of the seasonal (JJA) mean ground-level ozone mixing rations in 2017 and 2018. Figures S14
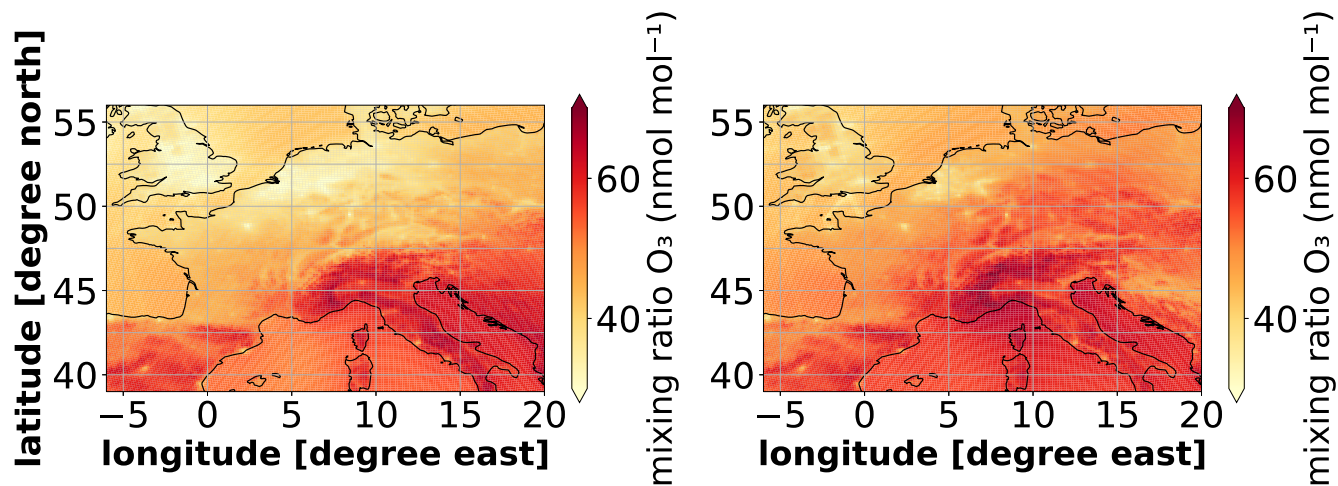and S15 show the absolute and relative contributions for JJA 2018.

Figure S13. Comparison of JJA ground-level ozone mixing ratios (in nmol mol^{-1}) in CM12 between the years 2017 (left) and 2018
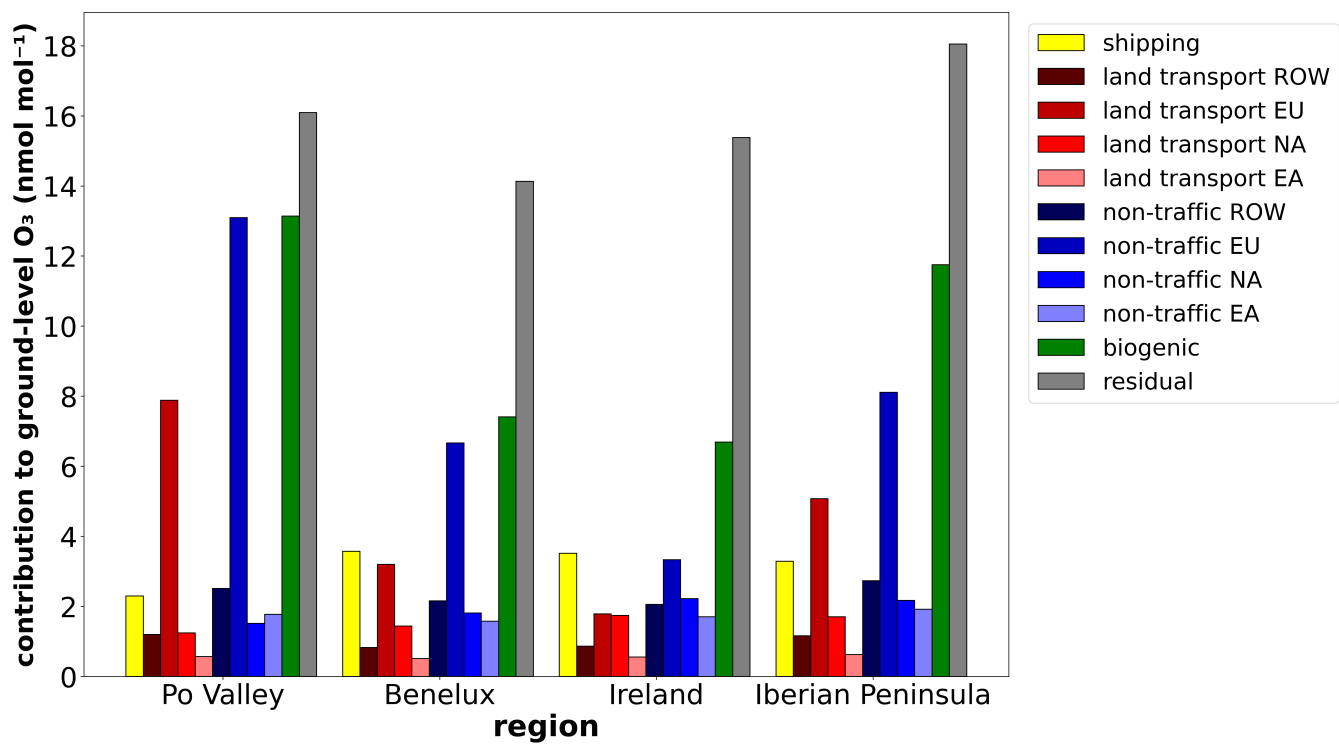(right).

Figure S14. Seasonal (JJA 2018) mean absolute contributions of different emission sectors and regions to ground-level ozone in the regions Benelux, Po Valley, West Ireland, and Iberian Peninsula for JJA 2018 as simulated with CM12.
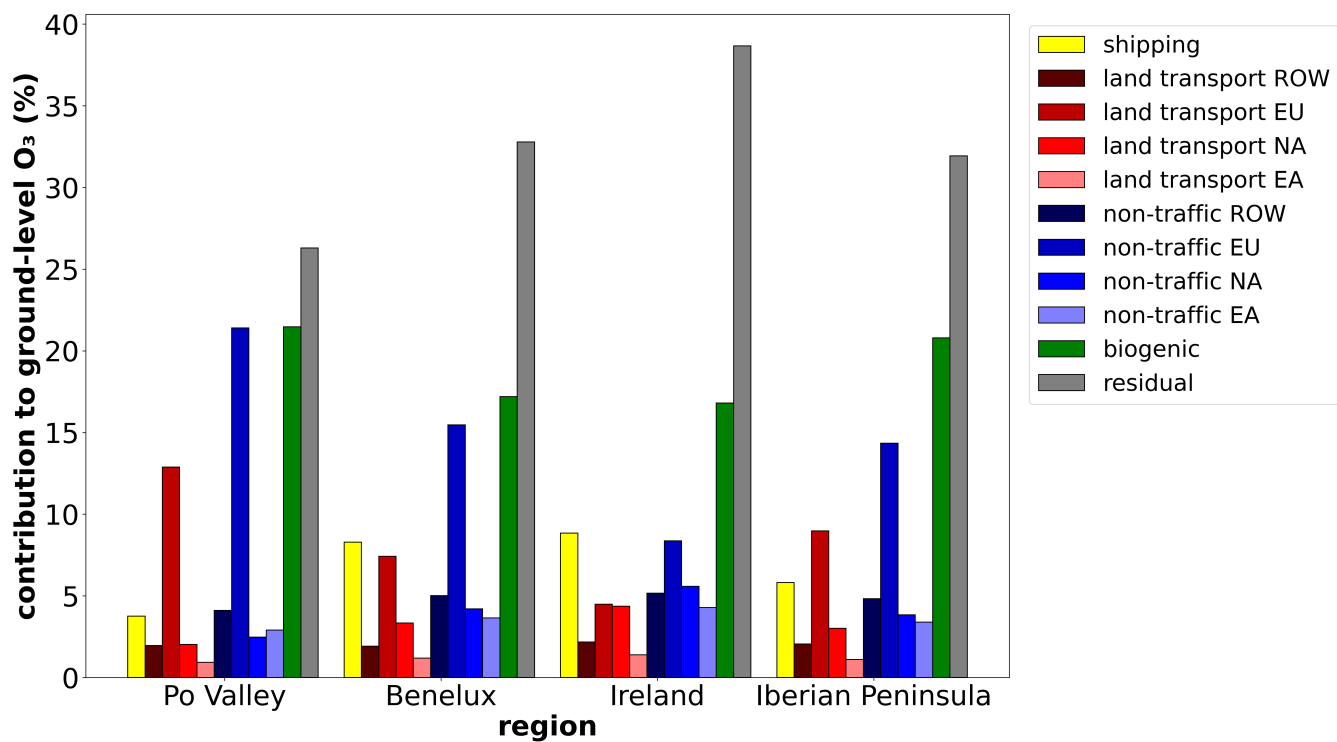
Figure S15. Seasonal (JJA 2018) mean relative contributions of different emission sectors and regions to ground-level ozone in the regions Po Valley, Benelux, West Ireland and Iberian Peninsula for JJA 2018 as simulated with CM12.

S8   Contributions to NO_y and NMHC

Figures S16 and S17 display the seasonal (JJA) mean contributions at ground-level to NO_y and NMHC, respectively.
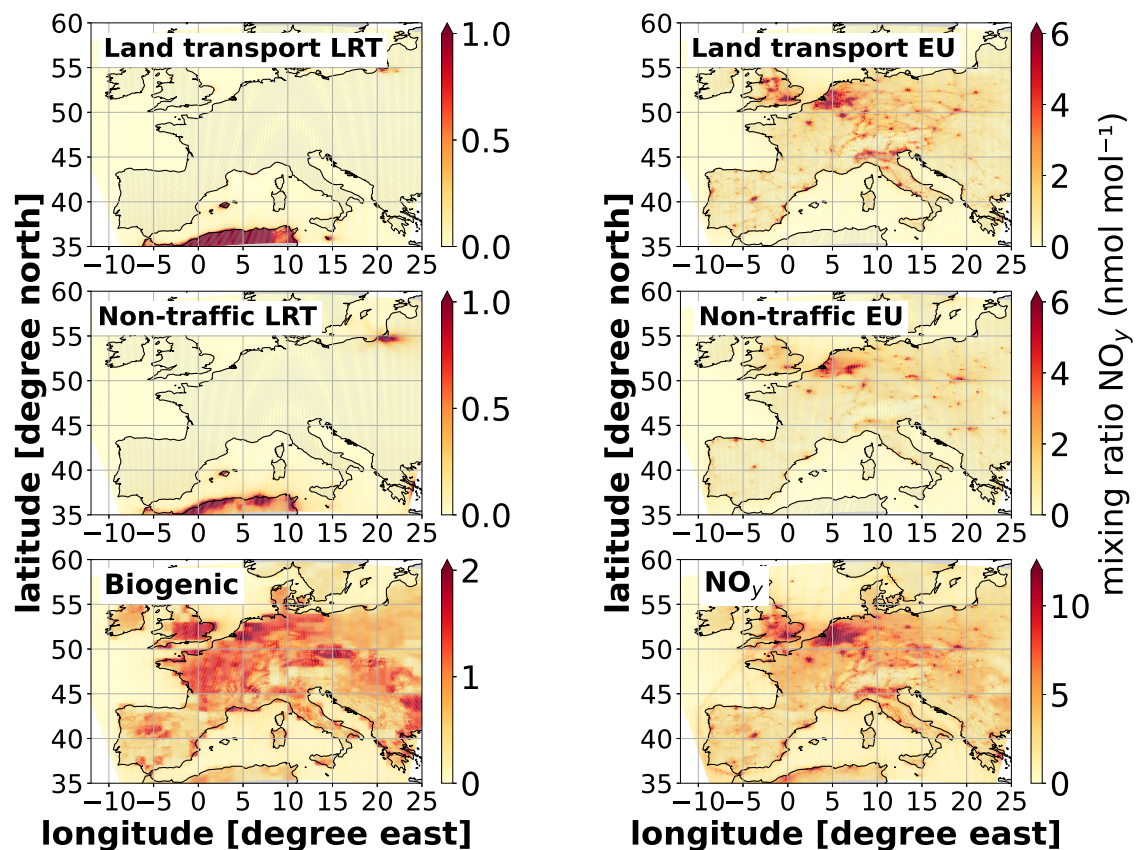

Figure S16. Seasonal (JJA 2017) mean absolute contributions of NO_y as mixing ratios in $nmol\ mol^{-1}$ from long-range transported (LRT: ROW + NA + EA) NO_y, biogenic emissions (for NO_y soil-NO_x), and European emissions by sectors, and total NO_y (lower right) as simulated with CM12. Please note the different colour scales for the individual plots.
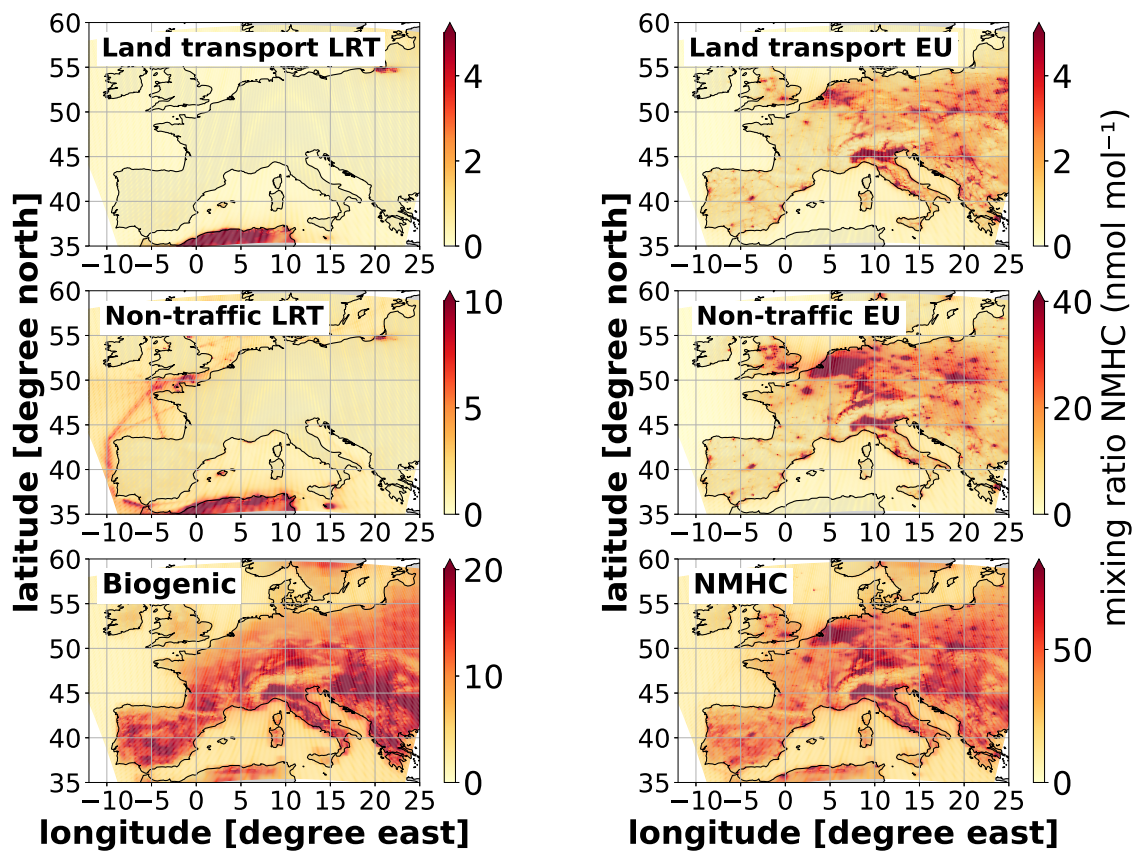
Figure S17. Seasonal (JJA 2017) mean absolute contributions of NMHC as mixing ratios in nmol mol^{-1} from long-range transported (LRT: ROW + NA + EA) NMHC, biogenic, and European emissions by sectors, and total NMHC (lower right) as simulated with CM12. Please note the different colour scales for the individual plots.
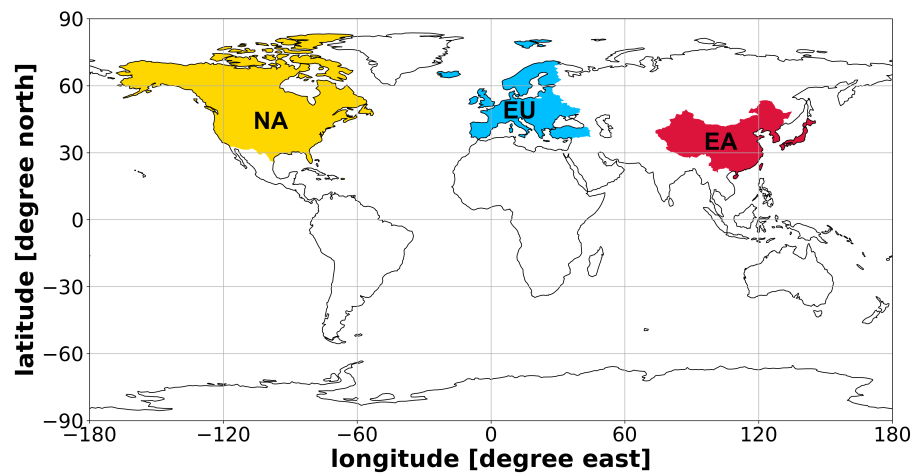
S9 Additional figures

Figure S18. Source regions (marked by color) for tagging in our MECO(2) model setup are defined as: North America (NA), Europe (EU) and East Asia (EA). All other countries and the ocean are considered as rest of the world (ROW).
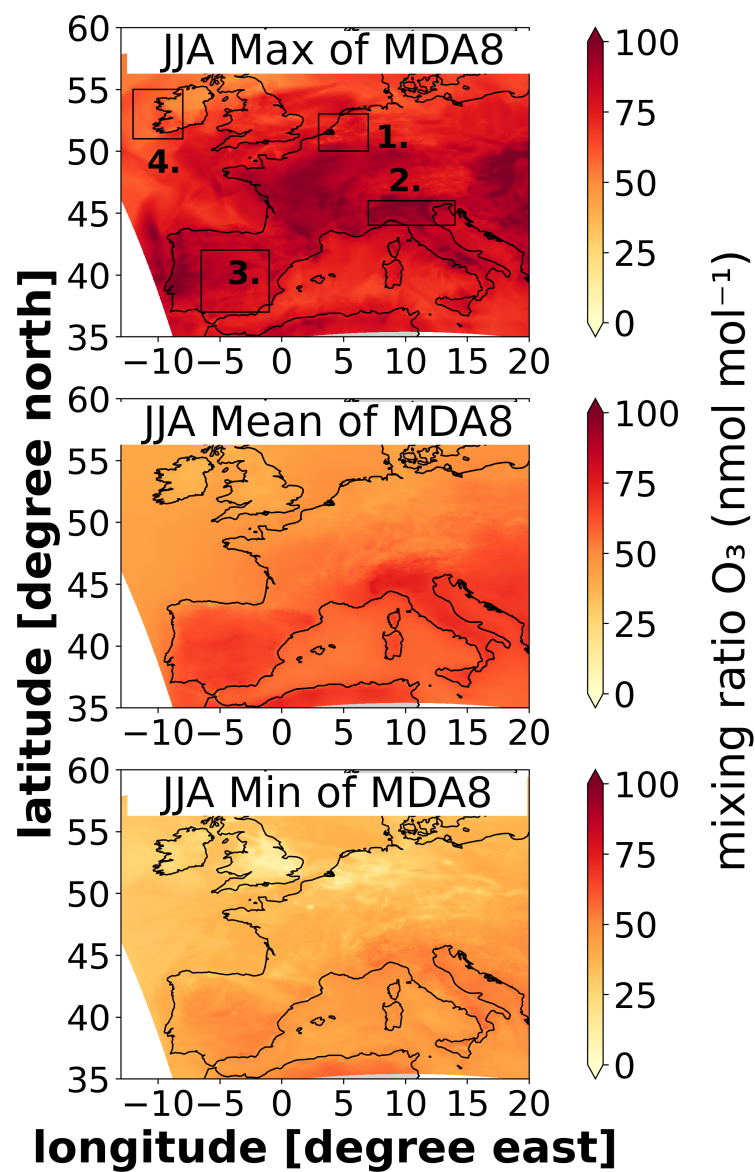
Figure S19. Maximum, Minimum and Mean maximum daily 8-h average (MDA8) mixing ratios in $nmol\ mol^{-1}$ based on 1-hourly model output from CM12 for JJA 2017. The black rectangles mark the study areas with 1. Benelux, 2. Po Valley, 3. Iberian Peninsula and 4. West Ireland.
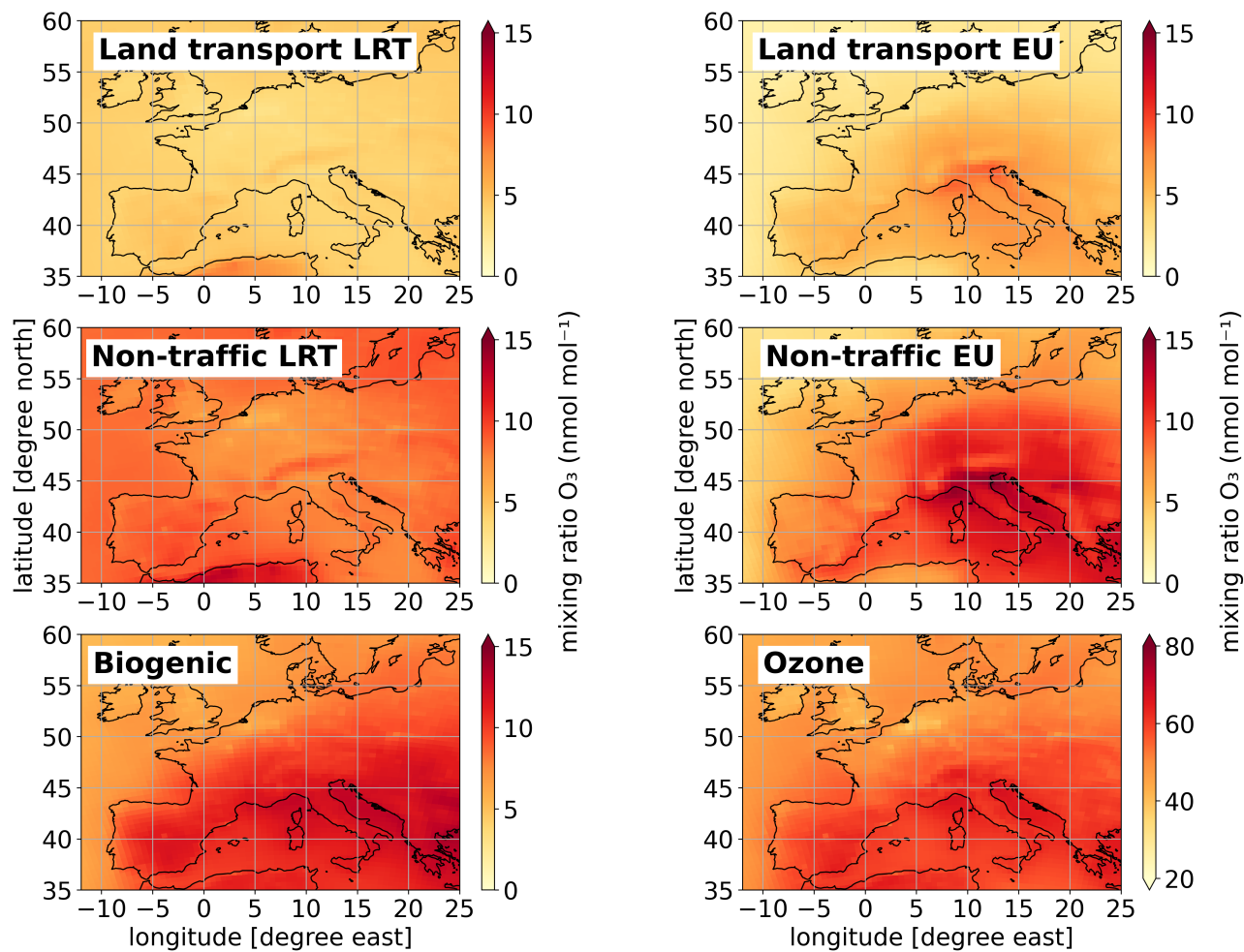
Figure S20. Seasonal (JJA 2017) mean absolute contribution as mixing ratios in $\mathrm{nmol\ mol^{-1}}$ of O_3 from long-range transported (LRT: ROW + NA + EA), biogenic, and European emissions, as simulated with CM50.
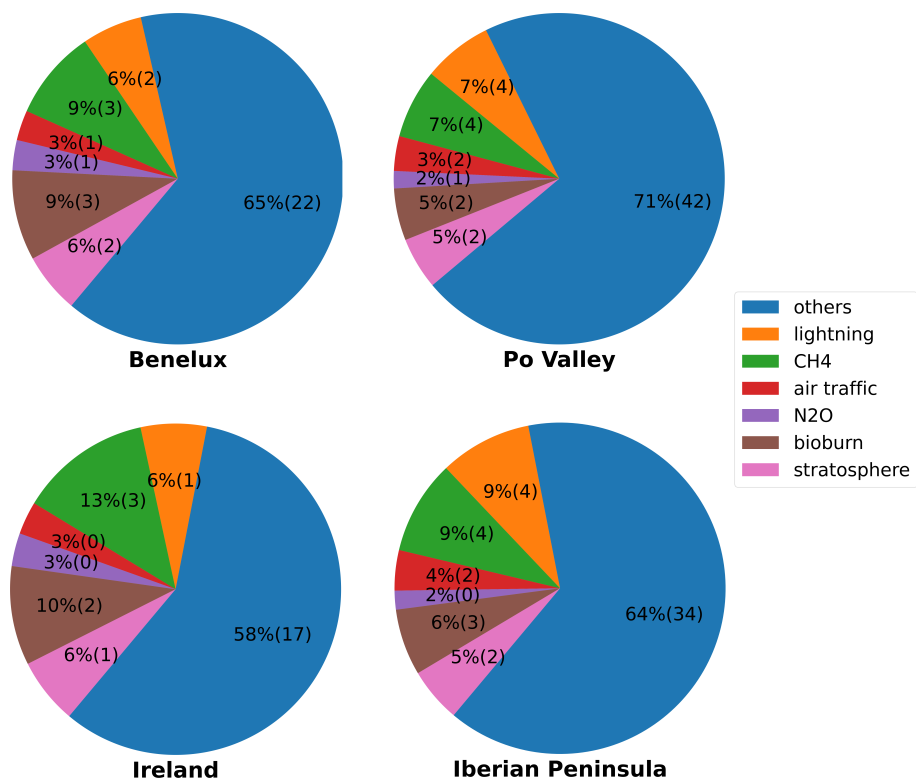
Figure S21. Absolute (parentheses) and relative, average (JJA 2017) contributions to ground level ozone, as mixing ratios in $\mathrm{nmol\ mol^{-1}}$ and %, respectively, of all sectors. The contributions are given for the regions Benelux, Po Valley, Iberian Peninsula and Ireland. Here, "Others" indicates the sum of the sectors land transport, anthropogenic non-traffic, shipping, and biogenic.

Figure S22. Box-whisker plot showing the monthly mean contributions of the most important emission sources at the 95th, 90th, and 75th percentiles of ozone as simulated by CM12 for JJA 2017. The first panel shows the relative contributions of O_3^{teu} and the sum of long-range transported relative contributions of O_3^{tra}, O_3^{tna} and O_3^{tea}. The second panel shows the relative contributions of O_3^{ieu} and the sum of long-range transported relative contributions of O_3^{ind}, O_3^{ina} and O_3^{iea}. The third panel shows the relative contributions of O_3^{soi}. The lower and upper ends of the boxes indicate the 25th and 75th percentiles of the corresponding regional distribution, respectively, the bar the median, and the whiskers are defined as ± 1.5 the interquartile range of the contributions of all grid boxes within the indicated region.
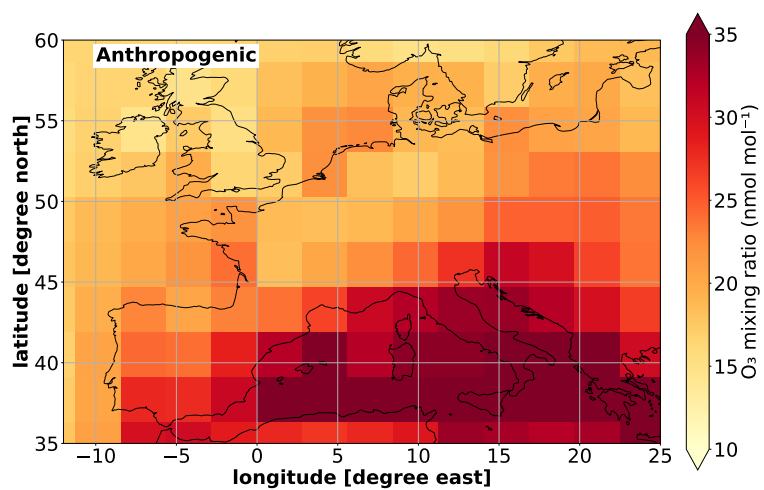
Figure S23. Mean absolute ozone contributions from anthropogenic emissions (land transport, non-traffic and shipping) in July 2017 in EMAC.

References

120   M. D. Andrés Hernández, A. Hilboll, H. Ziereis, E. Förster, O. O. Krüger, K. Kaiser, J. Schneider, F. Barnaba, M. Vrekoussis, J. Schmidt, H. Huntrieser, A.-M. Blechschmidt, M. George, V. Nenakhov, T. Harlass, B. A. Holanda, J. Wolf, L. Eirenschmalz, M. Krebsbach, M. L. Pöhlker, A. B. Kalisz Hedegaard, L. Mei, K. Pfeilsticker, Y. Liu, R. Koppmann, H. Schlager, B. Bohn, U. Schumann, A. Richter, B. Schreiner, D. Sauer, R. Baumann, M. Mertens, P. Jöckel, M. Kilian, G. Stratmann, C. Pöhlker, M. Campanelli, M. Pandolfi, M. Sicard, J. L. Gómez-Amo, M. Pujadas, K. Bigge, F. Kluge, A. Schwarz, N. Daskalakis, D. Walter, A. Zahn, U. Pöschl, H. Bönisch,

125   S. Borrmann, U. Platt, and J. P. Burrows. Overview: On the transport and transformation of pollutants in the outflow of major population centres – observational data from the emerge european intensive operational period in summer 2017. *Atmospheric Chemistry and Physics*, 22(9):5877–5924, 2022. https://doi.org/10.5194/acp-22-5877-2022.

Johannes Bieser, A. Aulinger, Volker Matthias, M. Quante, and Hugo Denier van der Gon. Vertical emission profiles for europe based on plume rise calculations. *Environmental pollution (Barking, Essex : 1987)*, 159:2935–46, 05 2011.

130   https://doi.org/10.1016/j.envpol.2011.04.030.

M. Delang, Jacob S Becker, Kai-Lan Chang, Marc L. Serre, Owen R. Cooper, Martin G. Schultz, Sabine Schröder, Xiao Lu, Lin Zhang, Makoto Deushi, Béatrice Josse, Christoph A. Keller, Jean-François Lamarque, Meiyun Lin, Junhua Liu, Virginie Marécal, Sarah A. Strode, Kengo Sudo, Simone Tilmes, Li Zhang, Stephanie E Cleland, Elyssa L Collins, Michael Brauer, and J. Jason West. Mapping yearly fine resolution global surface ozone through the bayesian maximum entropy data fusion of observations and model output for

135   1990-2017. *Environmental science & technology*, 2021.

F. Dentener, J. Drevet, J. F. Lamarque, I. Bey, B. Eickhout, A. M. Fiore, D. Hauglustaine, L. W. Horowitz, M. Krol, U. C. Kulshrestha, M. Lawrence, C. Galy-Lacaux, S. Rast, D. Shindell, D. Stevenson, T. Van Noije, C. Atherton, N. Bell, D. Bergman, T. Butler, J. Cofala, B. Collins, R. Doherty, K. Ellingsen, J. Galloway, M. Gauss, V. Montanaro, J. F. Müller, G. Pitari, J. Rodriguez, M. Sanderson, F. Solmon, S. Strahan, M. Schultz, K. Sudo, S. Szopa, and O. Wild. Nitrogen and sulfur deposition on regional and global scales: A multimodel evaluation.

140   model evaluation. *Glob. Biogeochem. Cycles*, 20:GB4003, 2006. https://doi.org/10.1029/2005GB002672.

European Environment Agency. Air quality e-reporting products on eea data service, 2018. https://www.eea.europa.eu/data-and-maps/data/aqereporting-8 (last access: 28 September 2022).

V. Grewe, E. Tsati, M. Mertens, C. Frömming, and P. Jöckel. Contribution of emissions to concentrations: the tagging 1.0 submodel based on the modular earth submodel system (messy 2.52). *Geoscientific Model Development*, 10(7):2615–2633, 2017.

145   https://doi.org/10.5194/gmd-10-2615-2017.

P. Jöckel, A. Kerkweg, A. Pozzer, R. Sander, H. Tost, H. Riede, A. Baumgaertner, S. Gromov, and B. Kern. Development cycle 2 of the modular earth submodel system (messy2). *Geoscientific Model Development*, 3(2):717–752, 2010. https://doi.org/10.5194/gmd-3-717-2010.

Bastian Kern. *Chemical interaction between ocean and atmosphere*. PhD thesis, Johannes Gutenberg-University Mainz, 11 2013.

150   S. Mailler, D. Khvorostyanov, and L. Menut. Impact of the vertical emission profiles on background gas-phase pollution simulated from the emep emissions over europe. *Atmospheric Chemistry and Physics*, 13(12):5987–5998, 2013. https://doi.org/10.5194/acp-13-5987-2013.

H. Ziereis, P. Hoor, J.-U. Grooß, A. Zahn, G. Stratmann, P. Stock, M. Lichtenstern, J. Krause, V. Bense, A. Afchine, C. Rolf, W. Woiwode, M. Braun, J. Ungermann, A. Marsing, C. Voigt, A. Engel, B.-M. Sinnhuber, and H. Oelhaf. Redistribution of total reactive nitrogen in the lowermost arctic stratosphere during the cold winter 2015/2016. *Atmospheric Chemistry and Physics*, 22(5):3631–3654, 2022.

155   https://doi.org/10.5194/acp-22-3631-2022. URL https://acp.copernicus.org/articles/22/3631/2022/.